A Novel 2-D Autofocusing Algorithm for Real Airborne Stripmap Terahertz Synthetic Aperture Radar Imaging

Yinwei Li, *Member, IEEE*, Jiawei Wu, Qianqian Mao, Han Xiao, Fei Meng, Wenquan Gao, and Yiming Zhu

Abstract— In practical applications, airborne terahertz synthetic aperture radar (THz-SAR) echo signal is not only affected by range amplitude and phase errors introduced by nonideal THz device but also affected by motion error in azimuth induced by the nonideal trajectory of platform, resulting in the 2-D defocus of image. To address the above errors, a novel 2-D autofocusing algorithm for real airborne stripmap THz-SAR imaging is proposed. In range autofocusing, the amplitude and phase errors are estimated simultaneously in range frequency domain based on the dominant point target selected in the preliminary focused images. To avoid dividing more subapertures in azimuth error estimate, the autofocusing method based on the maximization of image contrast is adopted. Then, range-Doppler algorithm (RDA) integrated with the proposed 2-D autofocusing is performed to obtain the focused images. The real measured data, acquired by a 0.22-THz airborne SAR system, are used to demonstrate the validity of the proposed algorithm. By comparing the imaging results, the proposed method can effectively and efficiently focus airborne stripmap THz-SAR images.

Index Terms— 2-D autofocusing algorithm, airborne stripmap terahertz synthetic aperture radar (THz-SAR), amplitude and phase error, contrast optimization.

I. INTRODUCTION

COMPARED with microwave synthetic aperture radar (SAR) imaging, terahertz SAR (THz-SAR) imaging has the advantages of higher resolution and higher frame rate, making it receive much more attention in the radar imaging fields [1], [2]. However, due to the nonideal characteristics of high-frequency multipliers and power amplifiers in the transmitting chains, THz-SAR transmitted signal is disturbed by amplitude and phase errors, which eventually results in a decrease in range resolution. Meanwhile, due to many factors, such as airflow disturbance, the echo signal of airborne THz-SAR system is also usually affected by motion errors in

Yinwei Li and Yiming Zhu are with the Terahertz Technology Innovation Research Institute, Terahertz Spectrum and Imaging Technology Cooperative Innovation Center, University of Shanghai for Science and Technology, Shanghai 200093, China (e-mail: liyw@usst.edu.cn; ymzhu@usst.edu.cn).

Jiawei Wu and Qianqian Mao are with the School of Optical-Electrical and Computer Engineering, University of Shanghai for Science and Technology, Shanghai 200093, China (e-mail: 203590543@st.usst.edu.cn; 212230413@st.usst.edu.cn).

Han Xiao, Fei Meng, and Wenquan Gao are with the Beijing Institute of Radio Measurement, Beijing 100854, China (e-mail: 520043801@qq.com; mengfei1028@sina.com; gaowenquan@sohu.com).

Digital Object Identifier 10.1109/LGRS.2023.3323266

azimuth, deteriorating the image focusing performance. The above 2-D errors are independent of each other, and it is essential to compensate them in real airborne THz-SAR imaging.

In general, the range dimensional errors are compensated after echo data acquisition. In [3], a nonlinear phase correction method based on time–frequency distribution is proposed. In [4], a nonlinear correction method for THz radar is proposed for solving range dependency of phase error. In [5], a nonlinear phase correction method is proposed for laser radar. In [6], a frequency nonlinearity correction method is proposed based on minimum entropy, but all these methods only consider the phase error, while the residual amplitude error still affects the image quality.

Besides, there are a few researches on high-frequency vibration error compensation of platform. Due to the lack of airborne THz-SAR measured data, only simulation verification is carried out [7], [8], [9], [10]. In fact, the motion errors for airborne THz-SAR are complicated, including not only high-frequency vibration error but also low-frequency motion error. In [11], a motion compensation method is proposed for vehicle borne THz-SAR based on subaperture decomposition, but if the subaperture division is not short enough, the performance will be degraded. In [12], a motion compensation method based on phase gradient autofocus (PGA) is proposed for airborne THz-SAR. However, when PGA is applied to stripmap SAR, the subaperture is required, and its length should be less than the synthetic aperture length (SAL) [13]. For THz-SAR, the shorter wavelength makes its SAL shorter. Therefore, when applying PGA to stripmap THz-SAR, more subapertures are needed for processing data of the same length, which increases the processing complexity.

To compensate 2-D errors of real airborne stripmap THz-SAR, a novel 2-D autofocusing algorithm is proposed. First, the range amplitude and phase errors are simultaneously estimated in range frequency domain. Then, the azimuth phase errors are estimated based on the maximization of defocus image contrast. By the above two steps, the compensation of all the errors is completed.

II. THz-SAR IMAGING SIGNAL MODEL WITH 2-D ERRORS

The imaging geometry of airborne stripmap THz-SAR is shown in Fig. 1. Ideally, the radar continuously transmits linear frequency modulation (LFM) signal and receives the echo signal at the interval of pulse repetition time when the radar platform moves horizontally along the X-direction with a constant speed of v and a reference height of H, but in practice, the LFM signal contains amplitude and phase error, and the platform deviates from the ideal trajectory, which both
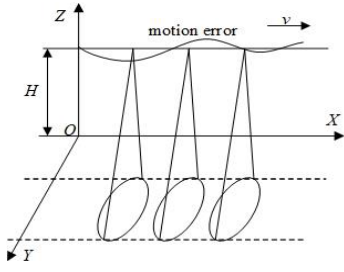
Fig. 1. Stripmap THz-SAR imaging geometry.

affects the echo signal. Letting the transmitted LFM signal be

$$s(\tau) = w_e(\tau) \cdot w_r(\tau) \exp\{j[2\pi f_c \tau + \pi K_r \tau^2 + e(\tau)]\} \quad (1)$$

where f_c is the signal carrier frequency, τ is the range fast time, K_r is the chirp rate, $w_r(\tau)$ is the signal envelope, and $w_e(\tau)$ and $e(\tau)$ denote the amplitude and phase error, respectively. After mixing demodulation, the received echo signal is expressed as

$$s_0(\tau, t) = w_r\left(\tau - \frac{2R(t)}{c}\right) w_a(t - t_0) \exp\left\{-j\frac{4\pi}{\lambda}R(t)\right\}$$
$$\cdot \exp\left\{j\pi K_r\left(\tau - \frac{2R(t)}{c}\right)^2\right\} \cdot s_e\left(\tau - \frac{2R(t)}{c}\right) \quad (2)$$

where t is the azimuth slow time, t_0 is the beam center crossing time, c is the light speed, λ is the wavelength, $w_a(t)$ is the azimuth signal envelope, $s_e(\tau, t) = w_e(\tau) \exp\{je(\tau)\}$, and the actual slant range $R(t)$ is the sum of ideal slant range $R_0(t)$ and slant range error $\Delta R(t)$

$$R(t) = R_0(t) + \Delta R(t) \cong r_0 + \frac{v^2(t - t_0)^2}{2r_0} + \Delta R(t). \quad (3)$$

Through performing Fourier transform (FT) to τ, according to the principle of stationary phase (POSP) and neglecting the contribution of $e(\tau)$ to the stationary point (SP) calculation, we obtain the signal expression in the range frequency domain

$$S_0(f_\tau, t) = w_a(t - t_0) \exp\left\{-j\frac{4\pi(f_c + f_\tau)}{c}R(t)\right\} \cdot w_r\left(\frac{f_\tau}{K_r}\right)$$
$$\cdot \exp\left\{-j\pi\frac{f_\tau^2}{K_r}\right\} \cdot S_e(f_\tau) \quad (4)$$

where $S_e(f_\tau) = w_e(f_\tau/K_r) \exp\{je(f_\tau/K_r)\}$.

After range matched filtering and applying inverse FT (IFT) to f_τ, we achieve the range compressed signal as

$$s_{rc}(\tau, t) = w_a(t - t_0) \exp\left\{-j\frac{4\pi}{\lambda}R_0(t)\right\} \exp\{-j\varphi(t)\}$$
$$\cdot \text{sinc}\left(\tau - \frac{2R_0(t)}{c}\right) \otimes_\tau \text{IFT}_{f_\tau}\{S_e(f_\tau)\} \quad (5)$$

where $\varphi(t) = 4\pi\Delta R(t)/\lambda$ is the phase error in azimuth dimension caused by the motion error, $\text{IFT}_{f_\tau}\{\cdot\}$ denotes the IFT to f_τ, and $\otimes_\tau$ is the convolution of time τ.

Then, azimuth FT is applied to (5), where POSP is also used and the contribution of $\varphi(t)$ to the SP calculation is also neglected. Thus, the range Doppler signal is expressed as

$$S_{rc}(\tau, f_t) = w_a\left(\frac{f_t}{K_a}\right) \exp\left\{j\left(\pi\frac{f_t^2}{K_a} - 2\pi f_t t_0\right)\right\}$$

$$\cdot \exp\left\{j\varphi\left(-\frac{f_t}{K_a}\right)\right\}$$
$$\cdot \text{sinc}\left(\tau - \frac{2r_0}{c} - \frac{2}{c}\frac{\lambda f_t^2}{4K_a}\right) \otimes_\tau \text{IFT}_{f_\tau}\{S_e(f_\tau)\}$$
$$\cdot \exp\left\{-j\frac{4\pi r_0}{\lambda}\right\} \quad (6)$$

where $K_a = (2v^2/\lambda r_0)$ denotes the azimuth chirp rate.

After performing range cell migration correction (RCMC) and azimuth matched filtering, azimuth IFT is applied to transfer the signal into 2-D image domain, which yields

$$s_{out}(\tau, t) = \text{sinc}\left(\tau - \frac{2r_0}{c}\right) \otimes_\tau \text{IFT}_{f_\tau}\{S_e(f_\tau)\}$$
$$\cdot \exp\left\{-j\frac{4\pi}{\lambda}r_0\right\} \cdot \text{sinc}(t - t_0)$$
$$\otimes_t \text{IFT}_{f_t}\left\{\exp\left\{j\varphi\left(-\frac{f_t}{K_a}\right)\right\}\right\} \quad (7)$$

where $\text{IFT}_{f_t}\{\cdot\}$ denotes the IFT with respect to $f_t \otimes_t$ is the convolution of time t. According to (7), the 2-D images are affected by range and azimuth errors, which degrades the image quality and seriously affect the image interpretation.

III. TWO-DIMENSIONAL AUTOFOCUSING ALGORITHM

A. Range Dimensional Autofocusing

In the estimation of range amplitude and phase error, the dominant point target in the imaging scene is first selected according to [14]. To improve the signal-to-noise ratio of the dominant point target, range-Doppler algorithm (RDA) is used to process the echo data. A preliminary focused image that is disturbed by 2-D errors is achieved. Then, according to the peak value position $((2r_0/c), t_0)$ of the dominant point target, the corresponding range compressed data sequence for the azimuth time t_0 is achieved, which can be expressed as

$$s_{out}(\tau) = \text{sinc}\left(\tau - \frac{2r_0}{c}\right) \otimes_\tau \text{IFT}_{f_\tau}\{S_e(f_\tau)\}. \quad (8)$$

To separate the dominant point target from other clutter, it is necessary to add window function to the dominant point target in the image domain. Letting the window function added be

$$w(\tau) = \text{rect}\left[\frac{\tau - 2r_0/c}{T}\right] \quad (9)$$

where

$$\text{rect}\left[\frac{\tau}{T}\right] = \begin{cases} 1, & |\tau| \leq T/2 \\ 0, & |\tau| > T/2. \end{cases}$$

Then, (8) can be rewritten as

$$s_{out}(\tau) = \text{sinc}\left(\tau - \frac{2r_0}{c}\right) \otimes_\tau \text{IFT}_{f_\tau}\{S_e(f_\tau)\} \cdot w(\tau). \quad (10)$$

Applying FT to (10), we have

$$S_{out}(f_\tau) = \text{rect}\left[\frac{f_\tau}{B}\right] \cdot S_e(f_\tau) \otimes_{f_\tau} \text{FT}_\tau\{w(\tau)\}. \quad (11)$$

$\text{FT}_\tau\{w(\tau)\}$ is a Sinc function and can be approximated as an impulse function $\delta(f_\tau)$. Hence, (11) can be simplified as

$$S_{out}(f_\tau) = \text{rect}\left[\frac{f_\tau}{B}\right] \cdot S_e(f_\tau). \quad (12)$$

TABLE I
THz-SAR SYSTEM PARAMETERS

Parameter	Value	Parameter	Value
Center frequency	220 GHz	View angle	60°
Platform height	500 m	Signal bandwidth	900 MHz
Platform speed	67 m/s	Sample frequency	1120 MHz
Pulse width	15 μs	Pulse repetition frequency	3333.3 Hz

In this way, the range amplitude and phase errors in range frequency domain are simultaneously estimated through

$$\begin{cases} \hat{w}_e(f_\tau) = |S_e(f_\tau)| = |S_{\text{out}}(f_\tau)| \\ \hat{e}(f_\tau) = \text{angle}(S_e(f_\tau)) = \text{angle}(S_{\text{out}}(f_\tau)). \end{cases} \tag{13}$$

Then, after range matched filtering with error compensation, the range compressed signal in (5) is rewritten as

$$s_{\text{rc}}(\tau, t) = \text{sinc}\left(\tau - \frac{2r_0}{c} - \frac{v^2 t^2}{cr_0}\right) w_a(t - t_0) \exp\left\{-j\frac{4\pi}{\lambda}r_0\right\}$$
$$\cdot \exp\left\{-j\pi K_a(t - t_0)^2\right\} \exp\left\{-j\varphi(t)\right\}. \tag{14}$$

B. Azimuth Dimensional Autofocusing

In the application of azimuth autofocusing algorithm, such as PGA or maximum contrast autofocus (MCA), to SAR imagery, the high order phase in (14) is first removed. After RCMC and deramping, we obtain

$$s_{de}(\tau, t) = s_i(\tau, t) \cdot \exp\{-j\varphi(t)\} \tag{15}$$

where $s_i(\tau, t)$ is the ideal deramped signal and $s_i(\tau, t) = \text{sinc}(\tau - (2r_0/c)) w_a(t - t_0) \exp\{j2\pi K_a t_0 t\} \exp\{-j(4\pi/\lambda)r_0\}$.

For microwave SAR, PGA is one of the most classical and effective autofocus methods, but it cannot be directly applied to stripmap SAR imagery. To apply PGA to the stripmap mode, an effective scheme is to split the azimuth whole data length into a series of subapertures and estimate the phase error for each subaperture independently. Since the scatterers in different positions span different segments of the phase error estimate, the subaperture length should be less than the SAL to make most scatterers in subaperture contain the phase information of the whole subaperture. Thus, the sampling points number of subaperture data processed by PGA each time should meet the conditions

$$N_{\text{PGA}} = \alpha \cdot T_a \cdot \text{PRF} = \alpha \cdot B_a / K_a \cdot \text{PRF} \tag{16}$$

where T_a is the synthetic aperture time, B_a is the Doppler bandwidth, PRF denotes the pulse repetition frequency and PRF $= (2 \sim 4)B_a$, and α is a constant factor and usually $1/2 \sim 3/4$.

Other well-known autofocus methods, such as MCA, take image focusing performance as the evaluation metric. When MCA is applied to stripmap SAR imagery, the length of azimuth data processed each time is limited by the fact that the image obtained by performing azimuth FT to (15) is not aliased. That is to say, the sampling points number of azimuth data processed each time should meet the conditions

$$N_{\text{MCA}} \leq \text{PRF}^2 / K_a. \tag{17}$$

Compared (16) and (17), it is clear that N_{MCA} is much larger than N_{PGA}. For example, based on the real airborne stripmap THz-SAR system, whose parameters are listed in Table I, the sampling points number of azimuth data processed each time N_{PGA} and N_{MCA} are about 170~260 and 1730, respectively.
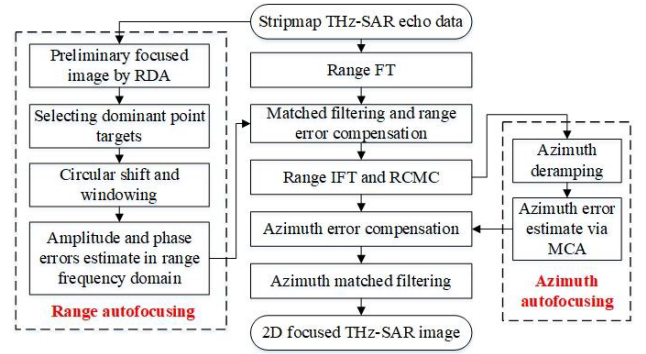

Fig. 2. Flowchart of the proposed 2-D autofocusing method.

Thus, for processing azimuth data of the same length, the number of subapertures divided by PGA is much larger than that of MCA, which inevitably increases the computational complexity. In addition, the PGA requires the presence of strong scatterers in each subaperture scene, which is usually not satisfied. Considering the above factors, the proposed 2-D autofocusing algorithm adopts MCA to realize azimuth phase error compensation.

Supposed that the compensated error in azimuth is $\exp\{j\phi(t)\}$, after azimuth error compensation, the azimuth focused SAR image can be expressed as

$$I(\tau, f_t) = \text{FT}_t\{s_{de}(\tau, t) \cdot \exp\{j\phi(t)\}\}. \tag{18}$$

The maximum contrast metric is applied to solve ϕ [15]

$$\hat{\phi} = \arg\max C_{\text{eq}}(\phi) \tag{19}$$

where $C_{\text{eq}}(\phi) = \int \int |I(\tau, f_t; \phi)|^4 d\tau \cdot df_t$.

There are many methods to solve the optimization problem in (19), e.g., Gauss–Newton method. Then, after compensating the error term, the azimuth uncompressed signal is rewritten as

$$s_{\text{rc}}(\tau, t) = \text{sinc}\left(\tau - \frac{2r_0}{c}\right) w_a(t - t_0) \exp\left\{-j\frac{4\pi}{\lambda}r_0\right\}$$
$$\cdot \exp\left\{-j\pi K_a(t - t_0)^2\right\}. \tag{20}$$

Finally, after azimuth matched filtering, we achieve the 2-D focused SAR image

$$I(\tau, t) = \text{sinc}\left(\tau - \frac{2r_0}{c}\right) \text{sinc}(t - t_0) \exp\left\{-j\frac{4\pi}{\lambda}r_0\right\}. \tag{21}$$

C. Procedure of the Proposed 2-D Autofocusing Method

To sum up, the whole procedure of the proposed novel 2-D autofocusing algorithm for real airborne stripmap THz-SAR imaging is summarized in Fig. 2.

IV. EXPERIMENTAL RESULTS

To verify the validity of the proposed method, real airborne THz-SAR measured data are performed. The data are acquired by 0.22-THz airborne stripmap SAR system, developed by the Beijing Institute of Radio Measurement. Table I gives the system parameters.

The imaging scene in test area 1 is a THz pattern composed of multiple corner reflectors. The azimuth length of raw data is 1400. When PGA is used for azimuth autofocusing, six to nine subapertures need to be divided for processing, but
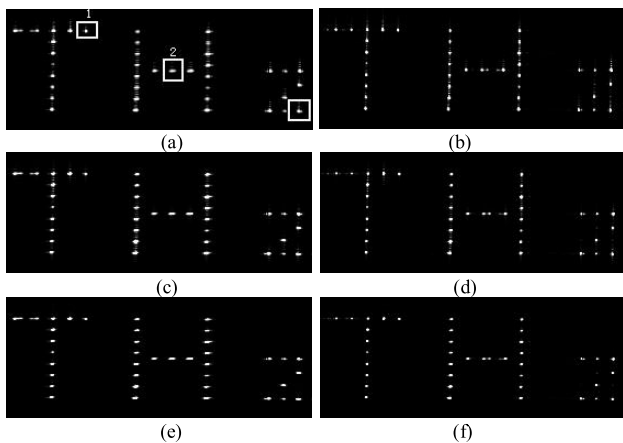
Fig. 3. THz-SAR imaging results of multiple corner reflectors. (a) Without autofocusing. (b) Azimuth autofocusing. (c) Range phase error compensation. (d) Range phase error compensation and azimuth autofocusing. (e) Range autofocusing. (f) Two-dimensional autofocusing.
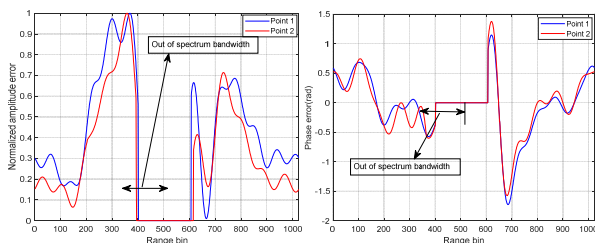

Fig. 4. (Left) Amplitude and (right) phase error in range frequency domain.
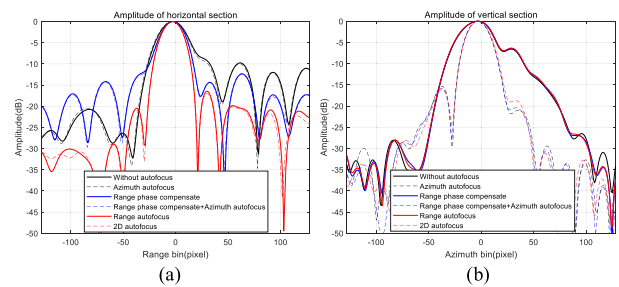

Fig. 5. Performance evaluation of point target in the bottom right of Fig. 2. (a) Range profile. (b) Azimuth profile.

TABLE II
PERFORMANCE VALUES COMPARISON

Range compressed image			Without autofocus	phase compensate	With autofocus
		Entropy	11.7191	11.5079	11.1746
		Contrast	2.5846	2.9513	3.4480
2-D image	Without autofocus	Entropy	7.0870	6.8292	6.3843
		Contrast	7.3747	8.3439	9.8132
	Azimuth autofocus	Entropy	6.7067	6.5660	6.1139
		Contrast	9.7673	10.6924	12.5647

no additional aperture is needed for the proposed algorithm. Fig. 3(a) shows the imaging result directly using RDA without autofocusing. The vertical and horizontal directions of SAR image denote the range and azimuth dimension, respectively. The imaging result is downsampled by five times in azimuth direction, and the image pixel size is 110×280. As can be seen from Fig. 3(a), THz-SAR image has an obvious 2-D defocus phenomenon. Then, the proposed autofocusing method is used to process it, in which the range amplitude and phase errors are extracted based on the point 1 circled in Fig. 3(a). Fig. 4 gives the estimated amplitude and phase error, and Fig. 3(f) gives the corresponding imaging result. Compared with Fig. 3(a), the quality of Fig. 3(f) has greatly improved. To verify the necessity of 2-D error compensation, Fig. 3(b)–(e) shows the imaging results of azimuth autofocusing, range phase error compensation, range phase error compensation and azimuth autofocusing, and range autofocusing, respectively. As can be seen, the SAR image with partial error compensation is better than the SAR image without autofocusing but is still worse than the SAR image with 2-D autofocusing. Meanwhile, Fig. 4 also gives the amplitude and phase error estimated based on point 2. We can see that the estimated range errors of different target are basically the same, which also shows that it is sufficient to use a single point target for range autofocusing.

Fig. 5 shows the range profile and azimuth profile of the point target circled in the lower right box of Fig. 3(a). After azimuth autofocusing, the range dimensional image quality basically does not change, and the azimuth resolution and the peak sidelobe ratio (PSLR) are improved from 0.1974 m and -6.5630 dB to 0.1378 m and -15.9890 dB, which agrees well with the theoretical value of 0.1363 m. When the range phase error is compensated only, the range resolution and PSLR

are improved from 0.2201 m and -9.7708 dB to 0.1935 m and -12.2959 dB, and the azimuth dimensional image quality has basically no change compared with Fig. 3(a). After range phase error compensation and azimuth autofocusing, the range dimensional image quality at this time has basically no change compared with Fig. 3(c), and the azimuth dimensional image quality reaches the level of Fig. 3(b). After range autofocusing, the range resolution and PSLR are improved to 0.1753 m and -17.0204 dB, which agrees well with the theoretical value of 0.1741 m. At this time, the azimuth dimensional image quality is basically unchanged compared with Fig. 3(a)–(c). After 2-D autofocusing, the 2-D resolution of the point target reaches the theoretical values, and the PSLRs are better than -16 dB. We can see that in order to obtain focused SAR images, 2-D autofocusing must be performed during imaging, and both amplitude and phase error compensation should be considered during range autofocusing. Finally, the image entropy and contrast values for Fig. 3 are listed in Table II. To illustrate the effect of range error compensation, the entropy and contrast values of range compressed image are also listed in Table II. As can be seen from Table II, all the entropy and contrast of the image are improved after the error compensation, which further validates the effectiveness of the proposed algorithm.

In another experiment, an airplane is used as a target. The azimuth length of raw data is 900. When PGA is used for azimuth autofocusing, four to six subapertures need to be divided for processing, but no additional aperture is needed for the proposed algorithm. In this experiment, range errors estimated in the first experiment are directly used to compensate. Fig. 6 shows the corresponding imaging results. Similarly, the vertical and the horizontal directions of SAR image denote the range and azimuth dimension, respectively. The imaging result is also downsampled by five times in azimuth direction, and the image pixel size is 130×180. By comparing the images of Fig. 6, we can see that the image sidelobe is still high if only range phase error compensation is performed, while it is well suppressed after both range amplitude and phase error are compensated.

Fig. 7 shows the range profile and azimuth profile of the point target circled in the center box of Fig. 6(f). It can be seen from Fig. 7(a) that the resolution and the PSLR are
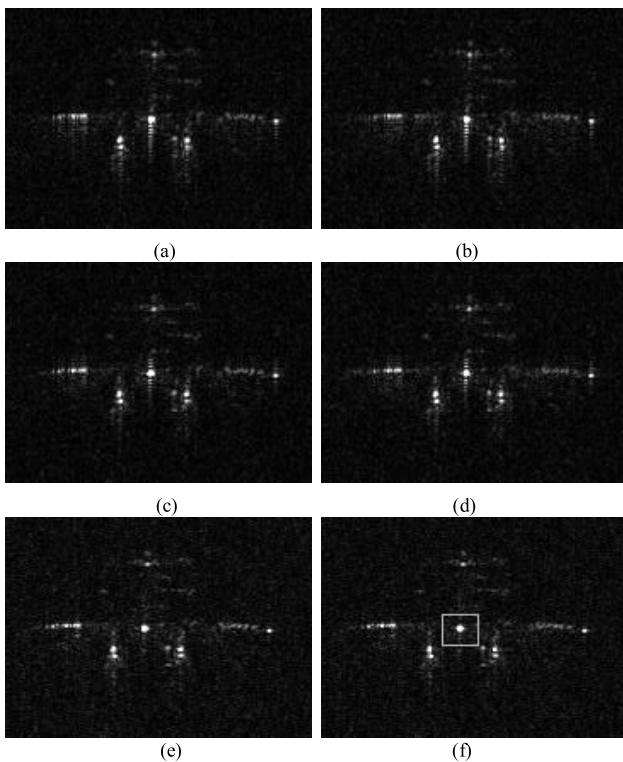
Fig. 6. THz-SAR imaging results of airplane. (a) Without autofocusing. (b) Azimuth autofocusing. (c) Range phase error compensation. (d) Range phase error compensation and azimuth autofocusing. (e) Range autofocusing. (f) Two-dimensional autofocusing.
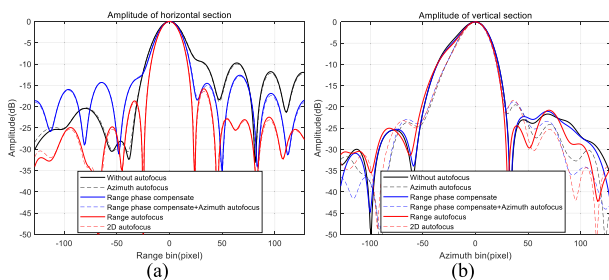

Fig. 7. Performance evaluation of point target in the center of Fig. 5. (a) Range profile. (b) Azimuth profile.

TABLE III
PERFORMANCE VALUES COMPARISON FOR FIG. 5

	(a)	(c)	(e)
Entropy	7.2683	7.1276	7.0102
Contrast	13.9565	15.8536	16.0115
	(b)	(d)	(f)
Entropy	7.2490	7.1002	7.0071
Contrast	15.3905	17.0278	17.1137

improved from 0.2135 m and -9.7473 dB to 0.1916 m and -12.8617 dB after range phase error compensation. After range autofocusing, they reach 0.1719 m and -16.4527 dB, respectively. The range resolution also agrees well with the theoretical value of 0.1741 m. This indicates that the THz-SAR system is relatively stable. Meanwhile, it can be seen from Fig. 7(b) that after azimuth autofocusing, the resolution is also improved from 0.1839 to 0.1549 m, which is basically consistent with the theoretical value of 0.1363 m. Finally, the image entropy and contrast values for Fig. 6 are listed in Table III. As can be seen from Table III, both the entropy

and contrast values of 2-D SAR images are improved, which validate the effectiveness of the proposed algorithm.

V. CONCLUSION

Due to the nonideal characteristics of THz devices and many factors, such as airflow disturbance in practice, the echo signal of a practical airborne THz-SAR system is usually affected by 2-D errors, which makes 2-D errors compensating be always challenging and essential for THz-SAR imaging. In this letter, a novel 2-D autofocusing algorithm is proposed for real airborne stripmap THz-SAR based on the dominant point target and MCA. In procedure of range autofocusing, the range amplitude and phase errors are simultaneously estimated in range frequency domain and they are used to compensate the whole stripmap THz-SAR echo data. Meanwhile, compared with PGA, MCA has no special requirements for the scene, and no additional subaperture is required. Finally, the two experimental data verify the effectiveness of the proposed algorithm.

REFERENCES

[1] S.-H. Kim, R. Fan, and F. Dominski, "ViSAR: A 235 GHz radar for airborne applications," in *Proc. IEEE Radar Conf.*, Apr. 2018, pp. 1549–1554.

[2] F. Zuo, J. Li, R. Hu, and Y. Pi, "Unified coordinate system algorithm for terahertz video-SAR image formation," *IEEE Trans. Terahertz Sci. Technol.*, vol. 8, no. 6, pp. 725–735, Nov. 2018.

[3] Y. Jiang, B. Deng, H. Wang, Y. Qin, and K. Liu, "An effective nonlinear phase compensation method for FMCW terahertz radar," *IEEE Photon. Technol. Lett.*, vol. 28, no. 15, pp. 1684–1687, Aug. 1, 2016.

[4] Y. Li, W. Hu, X. Zhang, Y. Zhao, J. Ni, and L. P. Ligthart, "A non-linear correction method for terahertz LFMCW radar," *IEEE Access*, vol. 8, pp. 102784–102794, 2020.

[5] R. Wang, M. Xiang, B. Wang, and C. Li, "Nonlinear phase estimation and compensation for FMCW ladar based on synchrosqueezing wavelet transform," *IEEE Geosci. Remote Sens. Lett.*, vol. 18, no. 7, pp. 1174–1178, Jul. 2021.

[6] J. Sheng, C. Fu, Q. Chen, Y. Li, and H. Wang, "A frequency nonlinearity and fluctuation correction method for terahertz ISAR imaging," in *Proc. China Int. SAR Symp. (CISS)*, Shanghai, China, Oct. 2018, pp. 1–4.

[7] Y. Zhang, J. Sun, P. Lei, and H. Wang, "High-frequency vibration compensation of helicopter-borne THz-SAR [correspondence]," *IEEE Trans. Aerosp. Electron. Syst.*, vol. 52, no. 3, pp. 1460–1466, Jun. 2016.

[8] Y. Li, L. Ding, Q. Zheng, Y. Zhu, and J. Sheng, "A novel high-frequency vibration error estimation and compensation algorithm for THz-SAR imaging based on local FrFT," *Sensors*, vol. 20, no. 9, p. 2669, May 2020.

[9] Y. Li, Q. Wu, J. Wu, P. Li, Q. Zheng, and L. Ding, "Estimation of high-frequency vibration parameters for terahertz SAR imaging based on FrFT with combination of QML and RANSAC," *IEEE Access*, vol. 9, pp. 5485–5496, 2021.

[10] J. Sun, Z. Hao, Q. Li, and D. Li, "Vibration compensation of airborne terahertz SAR based on along track interferometry," *IEEE Geosci. Remote Sens. Lett.*, vol. 19, pp. 1–5, 2022.

[11] S. Shi, C. Li, J. Hu, X. Zhang, and G. Fang, "Motion compensation for terahertz synthetic aperture radar based on subaperture decomposition and minimum entropy theorem," *IEEE Sensors J.*, vol. 20, no. 24, pp. 14940–14949, Dec. 2020.

[12] J. Chen, W. Wang, D. An, and Z. Zhou, "Airborne THz SAR imaging using RD algorithm integrated with autofocus," in *Proc. 6th Asia–Pacific Conf. Synth. Aperture Radar (APSAR)*, Nov. 2019, pp. 1–5.

[13] D. G. Thompson, J. S. Bates, D. V. Arnold, and D. G. Long, "Extending the phase gradient autofocus algorithm for low-altitude stripmap mode SAR," in *Proc. IEEE Int. Geosci. Remote Sens. Symp.*, Apr. 1999, pp. 564–566.

[14] H. Lim Chan and T. Soon Yeo, "Noniterative quality phase-gradient autofocus (QPGA) algorithm for spotlight SAR imagery," *IEEE Trans. Geosci. Remote Sens.*, vol. 36, no. 5, pp. 1531–1539, Sep. 1998.

[15] F. Berizzi and G. Corsini, "Autofocusing of inverse synthetic aperture radar images using contrast optimization," *IEEE Trans. Aerosp. Electron. Syst.*, vol. 32, no. 3, pp. 1185–1191, Jul. 1996.